



Improved thermoelectric properties of AgSbTe₂ based compounds with nanoscale Ag₂Te *in situ* precipitates

S.N. Zhang, T.J. Zhu*, S.H. Yang, C. Yu, X.B. Zhao

State Key Laboratory of Silicon Materials, Department of Materials Science and Engineering, Zhejiang University, Hangzhou 310027, PR China

ARTICLE INFO

Article history:

Received 28 December 2009

Received in revised form 18 March 2010

Accepted 18 March 2010

Available online 25 March 2010

Keywords:

Thermoelectric materials

Precipitation

Thermoelectric properties

Silver antimony tellurides

ABSTRACT

Ternary Ag_xSb_{2-x}Te_{3-x} thermoelectric materials have been prepared with x value varying from 0.78 to 0.93. By adjusting the Ag₂Te ratio, double-phased *in situ* nanocomposites were obtained with the nanostructured Ag₂Te embedded in the AgSbTe₂ matrix when $x > 0.81$. The high-resolution transmission electron microscopy observation showed that the Ag₂Te precipitates were *in situ* formed as nanodots and nanoscale lamellar structures. Compared with the single-phased samples of $x = 0.78$ and 0.81, the Seebeck coefficient of the nanocomposite samples exhibited significant improvement over the entire measured temperature range and the electrical conductivity also slightly increased, resulting in the increase of the power factor. At the same time, the thermal conductivity of the nanocomposite samples slightly decreased. The optimization of both the power factor and the thermal conductivity contributed to the notable improvement in figure of merit ZT by a factor of $\sim 40\%$ at 670 K.

© 2010 Elsevier B.V. All rights reserved.

1. Introduction

Thermoelectric (TE) materials have recently attracted more and more attentions due to the demands for alternative energy techniques to reduce our dependence on fossil fuels. TE devices can be used in the power generation mode based on the Seebeck effect and the refrigeration mode based on the Peltier effect [1,2]. The conversion efficiency of TE materials is represented by the dimensionless figure of merit, $ZT = \alpha^2 \sigma T / \kappa$, where α , σ , κ , and T are the Seebeck coefficient, the electrical conductivity, the thermal conductivity, and the absolute temperature, respectively [1].

As a p -type TE material, AgSbTe₂ has been reported since early 1960s [3–5]. Its lattice structure is widely considered to be the disordered NaCl-type with Ag and Sb randomly occupying the Na sites. But with a certain degree of Ag and Sb atomic ordering, the symmetry will be broken and tetragonal $P4mmm$ or primary cubic $Pm\bar{3}m$ structure can be formed [6–8]. Due to these structural characteristics, AgSbTe₂ reveals two distinct features as a thermoelectric material: the extremely low lattice thermal conductivity κ_L ($\sim 0.6 \text{ W m}^{-1} \text{ K}^{-1}$) and the relatively high Seebeck coefficient α ($\sim 200 \mu\text{V K}^{-1}$) [4,9]. Many theoretical studies, such as the lattice vibrational properties [10] and the electronic band structure [11] have been conducted for the long-time annealed stoichiometric AgSbTe₂. And other studies were mainly focused on the pseudo-binary phase diagram of Ag₂Te–Sb₂Te₃ [12]. In spite of all these

studies, due to the difficulty in controlling the phase components and the doping content, the optimization of TE properties is still marginal.

Recently, bulk TE nanocomposites have become a research hotspot due to the obvious enhancement in TE performance by nanostructuring [13–19] and their potential for large-scale commercial applications. There are mainly two types of TE nanocomposites according to the used approaches for the incorporation of nanostructures into bulk [15,20]. One is called the *ex situ* nanocomposites, such as Bi₂Te₃/Sb₂Te₃ [21], CoSb₃/Yb_{0.1}Co₄Sb₁₂ [22], CoSb₃/C60 [23], and ZrNiSn/ γ -Al₂O₃ [24], in which the nanoinclusions are mechanically incorporated into the bulk matrix and work as phonon scatter center to reduce the thermal conductivity. However, it is very hard to control the agglomeration, interface pollution and grain growth of nanoparticles during the preparation process. *In situ* TE nanocomposites, therefore, have been paid close attentions. Many efforts have recently been made to fabricate *in situ* nanocomposites. For example, Ge–Te based bulk *in situ* nanocomposites with 4–10 nm nanocrystals embedded in the amorphous matrix have been obtained by an amorphous crystallization method [15]. For the state-of-the-art mid-temperature thermoelectric system (PbTe) _{m} (AgSbTe₂) (denoted as LAST- m), a high figure of merit of >1.7 at 700 K was obtained due to the presence of *in situ* formed Ag–Sb-rich nanodots coherently embedded in the PbTe rich matrix [16,25–27]. Similar nanoscale microstructures have also been observed in (GeTe) _{x} (AgSbTe₂)_{100-x} (TAGS- x) system recently, which exhibited maximum ZT values of >1.5 at 800 K when $x = 80$ and 85 [28]. Among all the efforts on searching for suitable *in situ* nanocomposites systems, there are two meth-

* Corresponding author. Tel.: +86 571 87952181; fax: +86 571 87951451.
E-mail address: zhutj@zju.edu.cn (T.J. Zhu).

ods needed to highlight. One is the decomposition of metastable $\text{Pb}_2\text{Sb}_6\text{Te}_{11}$ into PbTe and Sb_2Te_3 . A layered self-assembly structure of PbTe and Sb_2Te_3 was produced [29]. The other is based on the peritectic process in the pseudo-binary phase diagram of Mg_2Si and Mg_2Sn . $\text{Mg}_2(\text{Si},\text{Sn})$ nanocomposites have been obtained with nanosized Mg_2Sn -rich phase coated on the microsized Mg_2Si -rich grains [20].

AgSbTe_2 can be recognized as the solid solutions between Ag_2Te and Sb_2Te_3 , and the single-phased AgSbTe_2 can only be obtained in a certain composition range with $\text{Ag}_2\text{Te}/\text{Sb}_2\text{Te}_3$ ratio smaller than 1 [12,30,31]. Utilizing the change in solid solubility near the single-phase region boundaries, it is possible to synthesize the *in situ* composites with Ag_2Te or Sb_2Te_3 embedded in the AgSbTe_2 matrix. What we need to do is to control the $\text{Ag}_2\text{Te}/\text{Sb}_2\text{Te}_3$ ratio near the single-phase region boundaries for obtaining the desirable nanocomposites of $\text{AgSbTe}_2/\text{Ag}_2\text{Te}$ or $\text{AgSbTe}_2/\text{Sb}_2\text{Te}_3$. In our previous study, the compositions with Sb_2Te_3 precipitates have been systematically studied [8]. In this paper, we investigate the compositions with higher Ag_2Te ratios. Single-phased AgSbTe_2 was fabricated as a reference within the composition range of $x = 0.78\text{--}0.81$ in $(\text{Ag}_2\text{Te})_x(\text{Sb}_2\text{Te}_3)_{1-x}$. We found that by increasing the $\text{Ag}_2\text{Te}/\text{Sb}_2\text{Te}_3$ ratio, the AgSbTe_2 composites were formed with Ag_2Te nanodots and lamellar precipitates. All the three TE parameters, namely α , σ and κ , could be optimized at certain Ag_2Te ratios, leading to the improvement in the TE performance of AgSbTe_2 nanocomposites.

2. Experimental

Stoichiometric amounts of single element Ag, Sb and Te with 99.999% purity were weighed and mixed as the nominal compositions of $\text{Ag}_x\text{Sb}_{2-x}\text{Te}_{3-x}$ ($(\text{Ag}_2\text{Te})_{x/2}(\text{Sb}_2\text{Te}_3)_{1-x/2}$), $x = 0.78, 0.81, 0.84, 0.87, 0.90$, and 0.93 , corresponding to 39%, 40.5%, 42%, 43.5%, 45%, and 46.5% Ag_2Te in atomic ratio, respectively. The mixtures were sealed in the evacuated quartz ampoules, and kept at 1273 K for 10 h. During this period, the ampoules were rocked several times to ensure good homogeneity of melts. The melts in the ampoules were then quenched by immersion into liquid nitrogen. The solidified ingots were crushed and pulverized to the particles of $<50 \mu\text{m}$. The final pellets with the diameter of $\varnothing 12.7 \text{ mm}$ and thickness of $\sim 1.5 \text{ mm}$ were obtained by hot pressing in a graphite die at 623 K under 70 MPa for 30 min in vacuum. The resultant pellet density is $95 \pm 2\%$ of the theoretical density for all the samples.

The powder X-ray diffraction (XRD) patterns were taken on a PANalytical X'Pert PRO diffractometer with $\text{Cu K}\alpha$ ($\lambda = 1.5402 \text{ \AA}$) radiation. The compositional analysis and mapping were taken by Inca-X-Stream energy-dispersive x-ray spectroscopy (EDX). Optical microscope images were shot on a Leica DM2500 M microscope. Transmission electron microscopy (TEM) samples were prepared by a grinding, dimpling, and ion milling (Gatan PIPS) process. The high-resolution transmission electron microscopy (HRTEM) images were obtained using a JEOL JEM-2010 microscope. The electrical conductivity σ and the Seebeck coefficient α were measured in the temperature range between 300 and 670 K on a computer-aided apparatus in argon using a DC four-probe method and differential voltage/temperature technique, respectively. The thermal diffusivity D and specific heat capacity C_p were measured on the samples of $\varnothing 12.7 \times 1.5 \text{ mm}^2$ by laser flash apparatus (LFA 457, Netzsch) with a Pyroceram standard. The accuracy for D and C_p measurements is about $\pm 3\%$ and $\pm 5\%$, respectively. The thermal conductivity was calculated by $\kappa = \rho C_p D$, where ρ is the density of samples. The Hall coefficient measurement was performed on a Quantum Design PPMS-9T system using the four-probe configuration with magnetic field sweeping between $\pm 4.0 \text{ T}$ at room temperature.

3. Results and discussion

The XRD patterns of the $\text{Ag}_x\text{Sb}_{2-x}\text{Te}_{3-x}$ ($x = 0.78\text{--}0.93$) samples are shown in Fig. 1(a). Two single-phased samples were obtained as $\text{Ag}_{0.78}\text{Sb}_{1.22}\text{Te}_{2.22}$ and $\text{Ag}_{0.81}\text{Sb}_{1.19}\text{Te}_{2.19}$, while the other four samples with $x > 0.81$ were double-phased. All the major diffraction peaks could be indexed into a face centered cubic $Fm\text{-}3m$ NaCl-type AgSbTe_2 structure (JCPDS Card No. 15-0540). While the minor phase in the double-phased samples, as pointed out by the black arrows, could be indexed into monoclinic $\alpha\text{-Ag}_2\text{Te}$ (JCPDS Card No. 34-0142). The characteristic regions have been enlarged and

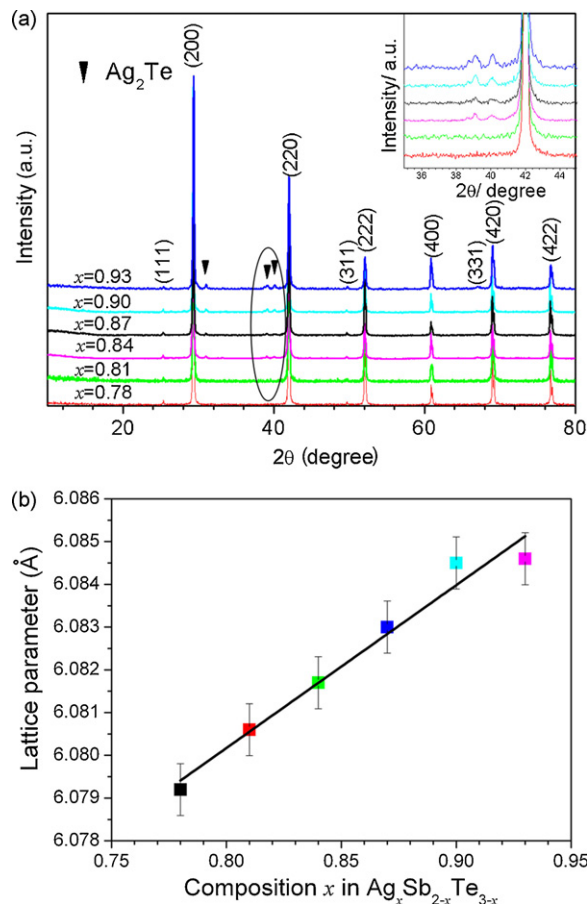


Fig. 1. (a) Powder X-ray diffraction patterns of $\text{Ag}_x\text{Sb}_{2-x}\text{Te}_{3-x}$ ($x = 0.78\text{--}0.93$) samples. The patterns from 2θ $35.5\text{--}44.5^\circ$ are magnified in the inset to show the precipitated Ag_2Te . (b) Composition dependence of lattice parameter fitted by Rietveld method.

shown in the inset. The Ag_2Te peaks in the double-phased samples increase with increasing x value. These XRD patterns have been fitted by Rietveld method to calculate the lattice parameters [32]. As shown in Fig. 1(b), the lattice parameters of AgSbTe_2 underwent a slight increase from 6.079 to 6.085 Å corresponding to the increase of Ag_2Te ratio. However, Fig. 1(b) suggests that the solubility of Ag_2Te goes up to some $x = 0.9$, inconsistent with the XRD patterns. A possible explanation is that the composition of the matrix keeps changed even after Ag_2Te precipitates. That means that both the matrix and precipitates are nonstoichiometric. More studies are needed.

The distributions of the precipitated Ag_2Te phase were studied from micro- to nanoscale. As shown in the optical microscopy image (Fig. 2(a)), the secondary phase precipitates can be observed clearly at the grain boundaries. The EDX mapping images in Fig. 2(b) confirmed that the grain boundary areas are rich in Ag and lack of Sb. Combining the XRD results, one can suggest that the precipitates are the Ag_2Te phase. More details can be seen in the HRTEM images from Fig. 2(c)–(f). In Fig. 2(c) and (d), Ag_2Te precipitates are formed as nanodots with the diameter of 10–30 nm. The lattice interspacing was measured to be $\sim 2.15 \text{ \AA}$, which corresponds to the (021) plane of monoclinic Ag_2Te . According to the previous study by Sugar and Medlin [33], these fine structures are caused by the solid-state precipitation. At the same time, there are also lamellar Ag_2Te , the thickness of which varies from 30 to 100 nm when the composition changes from $\text{Ag}_{0.84}\text{Sb}_{1.16}\text{Te}_{2.16}$ to $\text{Ag}_{0.90}\text{Sb}_{1.10}\text{Te}_{2.10}$ as shown in Fig. 2(e) and (f). The formation of these Ag_2Te lamellas can be related to the eutectic solidification [34]. As shown in

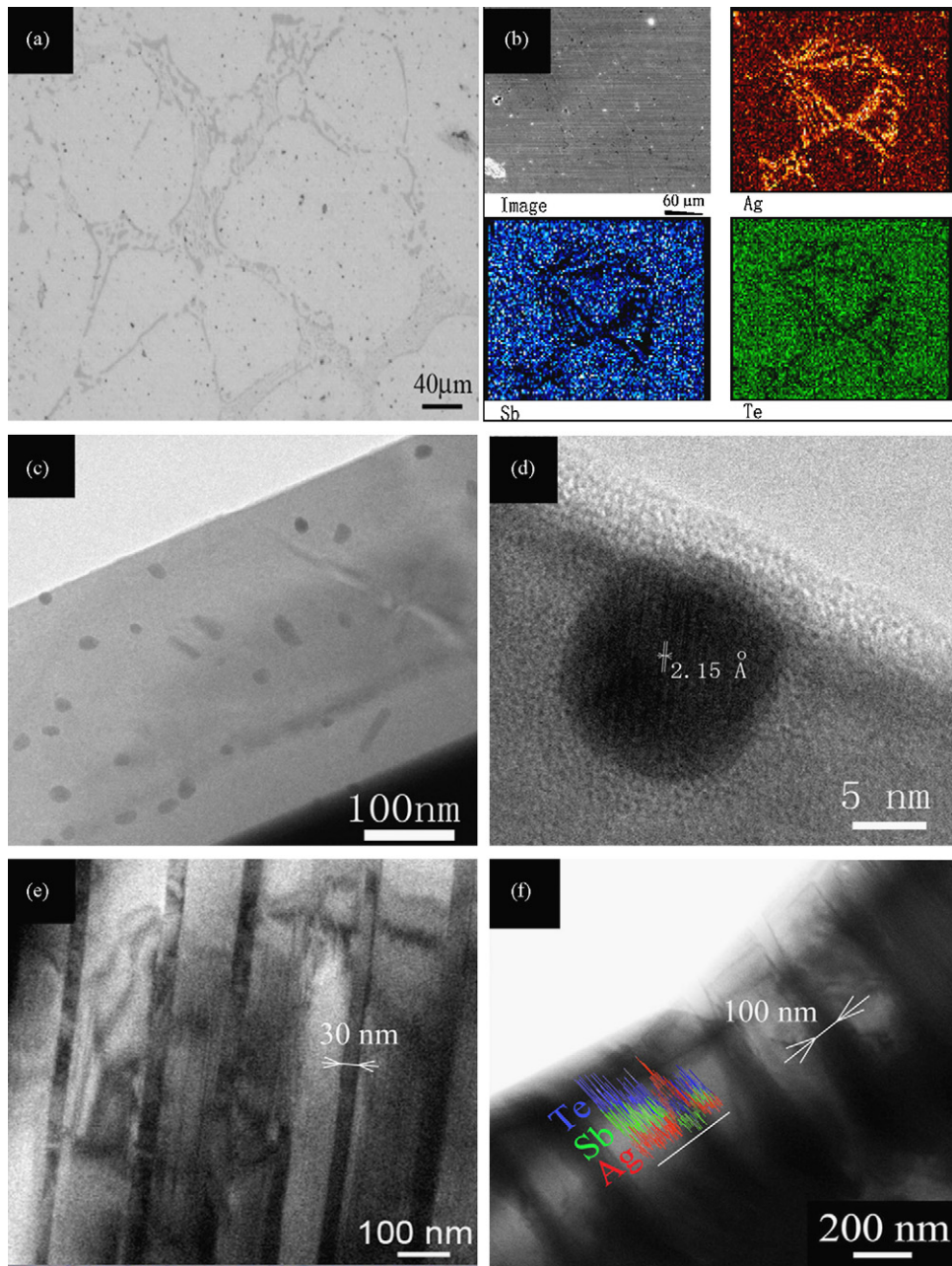


Fig. 2. Microstructures of Ag_2Te precipitated AgSbTe_2 sample. (a) Optical microscopy picture and (b) EDX mapping images of Ag, Sb, Te elements of $\text{Ag}_{0.84}\text{Sb}_{1.16}\text{Te}_{2.16}$. (c) and (d) Typical nanodots dispersed in the matrix of $\text{Ag}_{0.87}\text{Sb}_{1.13}\text{Te}_{2.13}$. (e) HRTEM image for $\text{Ag}_{0.84}\text{Sb}_{1.16}\text{Te}_{2.16}$. (f) HRTEM image and EDX line scanning for Ag, Sb and Te for $\text{Ag}_{0.90}\text{Sb}_{1.10}\text{Te}_{2.10}$.

Fig. 2(f), the composition difference between these lamellae and the matrix can be detected by EDX line scanning.

The temperature dependences of electrical transport properties of $\text{Ag}_x\text{Sb}_{2-x}\text{Te}_3$ ($x=0.78\text{--}0.93$) are shown in Fig. 3. The negative temperature dependence of electrical conductivity exhibited typical degenerate semiconductor behavior. As shown in Fig. 3, the temperature dependence of electrical conductivity of the two single-phased samples follows a power law of $\sigma \sim T^{-1/2}$ and $\sigma \sim T^{-1/3}$ for $\text{Ag}_{0.78}\text{Sb}_{1.22}\text{Te}_{2.22}$ and $\text{Ag}_{0.81}\text{Sb}_{1.19}\text{Te}_{2.19}$, respectively. This mostly reflects the $T^{-1/2}$ dependence of the mobility μ and the predominant acoustic phonon scattering in the samples with the scattering factor r of $\sim 1/2$ [34]. With increasing the content of precipitated Ag_2Te , the electrical conductivity slightly increased and then decreased. Therefore slight Ag_2Te precipitates are beneficial for the electrical transport. With further increasing Ag_2Te

content to $x=0.93$, the phase boundary scattering was enhanced and the introduced n -type minority concentration (induced by Ag_2Te) influenced the major hole transport. As a result the electrical conductivity decreased. A discontinuity could be observed on the curve of each double-phased sample, which is caused by a reversible phase transition from monoclinic $\alpha\text{-Ag}_2\text{Te}$ to cubic $\beta\text{-Ag}_2\text{Te}$ at 418 K. This phase transition has also been detected by DSC scan shown in the inset of Fig. 3. It is noteworthy that the DSC scan of single-phased samples without Ag_2Te precipitates has also been done (not shown here) and no detectable phase transition could be found, confirming that the DSC peak in the inset of Fig. 3 is due to the phase transition of Ag_2Te .

To explain the electrical transport behavior in this system, the Hall carrier concentration n and the mobility μ was measured on these samples, and the results are listed in Table 1. Due

Table 1
Room temperature physical properties for $\text{Ag}_x\text{Sb}_{2-x}\text{Te}_{3-x}$ ($x = 0.78, 0.81, 0.84, 0.87, 0.90$, and 0.93).

| x in $\text{Ag}_x\text{Sb}_{2-x}\text{Te}_{3-x}$ | 0.78 | 0.81 | 0.84 | 0.87 | 0.90 | 0.93 |
|---|------|------|------|------|------|------|
| Electrical conductivity (σ , 10^4 Sm^{-1}) | 3.48 | 2.63 | 2.69 | 2.79 | 2.33 | 1.89 |
| Seebeck coefficient (α , $\mu\text{V K}^{-1}$) | 188 | 231 | 295 | 250 | 281 | 254 |
| Carrier concentration (n , 10^{19} cm^{-3}) | 11.0 | 3.25 | 1.17 | 1.55 | 4.23 | 8.73 |
| Mobility (μ , $\text{cm}^{-2} \text{ V}^{-1} \text{ s}^{-1}$) | 15 | 51 | 144 | 112 | 34 | 14 |
| Effective mass (m^*/m_0) | 1.60 | 0.80 | 0.45 | 0.50 | 1.01 | 1.62 |

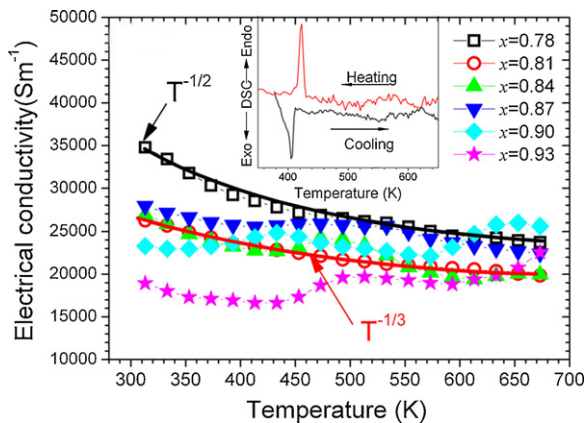


Fig. 3. Temperature dependence of electrical conductivity for $\text{Ag}_x\text{Sb}_{2-x}\text{Te}_{3-x}$ ($x = 0.78, 0.81, 0.84, 0.87, 0.90$, and 0.93).

to the carrier-carrier scattering, the mobility exhibited contrary composition dependence with carrier concentration. According to previous study, the p -type carriers in AgSbTe_2 are mainly caused by Ag vacancies [11]. So the maximum carrier concentration of $1.1 \times 10^{20} \text{ cm}^{-3}$ was obtained with the minimum Ag_2Te ratio of $x = 0.78$. With the further increase of x value from 0.81 to 0.90, the carrier concentration changed slightly. While the mobility increased due to the decrease of carrier concentrations. So the electrical conductivity remained the comparable value with that of the single-phased samples. For $\text{Ag}_{0.93}\text{Sb}_{1.07}\text{Te}_{2.07}$, the carrier concentration increased again to $8.73 \times 10^{19} \text{ cm}^{-3}$ and the mobility reduced to the minimum value of $14 \text{ cm}^{-2} \text{ V}^{-1} \text{ s}^{-1}$, which contributes to the obvious decrease of electrical conductivity for this sample.

The Seebeck coefficient α , shown in Fig. 4, is positive over the entire temperature range. For the two single-phased samples, the room temperature Seebeck coefficient increased from 190 to $230 \mu\text{V K}^{-1}$ with increasing Ag content. After the precipitation of Ag_2Te nanodots and lamellas, all the Seebeck coefficient

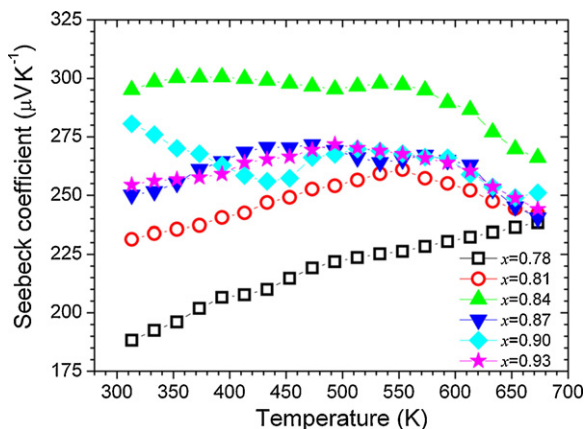


Fig. 4. Temperature dependence of Seebeck coefficient for $\text{Ag}_x\text{Sb}_{2-x}\text{Te}_{3-x}$ for $x = 0.78, 0.81, 0.84, 0.87, 0.90$, and 0.93 .

of double-phased samples exhibited a further increase and the temperature dependences of the Seebeck coefficient for double-phased samples are quite small over the entire temperature range. The maximum Seebeck coefficient of $300 \mu\text{V K}^{-1}$ was obtained for the $\text{Ag}_{0.84}\text{Sb}_{1.16}\text{Te}_{2.16}$ sample at room temperature.

There are several potential reasons for the increase of Seebeck coefficient. One of them is the increase in effective mass in the composites for the samples with higher Ag_2Te ratios. Using a parabolic band model, the effective masses m^* of these samples can be estimated with the equations below [35]:

$$\alpha = \frac{k_B}{e} \left[\eta_F - \frac{(r+5/2)F_{r+3/2}(\eta_F)}{(r+3/2)F_{r+1/2}(\eta_F)} \right] \quad (1)$$

$$n = 4\pi \left(\frac{2m^*k_B T}{h^2} \right)^{3/2} F_{1/2}(\eta_F) \quad (2)$$

$$F_i(\eta_F) = \int_0^\infty \frac{x^i dx}{1 + e^{(x-\eta_F)}}, \quad \eta_F = E_F / (k_B T) \quad (3)$$

where, $F_i(\eta_F)$ is the Fermi-Dirac integral expressed as equation (3), η_F is the reduced Fermi level function, i is the scattering factor, which has been proved to be $-1/2$ here for acoustic phonon scattering. E_F , k_B , h , and e are Fermi Energy, Boltzmann constant, Planck constant and electronic charge, respectively. m^* is the effective mass. The effective masses were calculated and listed in Table 1. The maximum Seebeck coefficient value of $\sim 300 \mu\text{V K}^{-1}$ was obtained at $\text{Ag}_{0.84}\text{Sb}_{1.16}\text{Te}_{2.16}$ with minimum effective mass of $0.45m_0$. So the enhancement in Seebeck coefficient is not because of the increase of effective mass. The possible reason of the increase in Seebeck coefficient may be attributed to the electron filtering effect caused by the nanoscale microstructure [36].

The power factors $PF = \alpha^2 \sigma$ as a function of temperature are plotted in Fig. 5. Compared with the single-phased samples, the power factors of the first three double-phased samples increased mainly due to the higher Seebeck coefficient, indicating the enhancement of the electrical transport properties after the precipitation of nanoscale Ag_2Te . The maximum power factor of $2.35 \times 10^{-3} \text{ W m}^{-1} \text{ K}^{-2}$ was obtained at 300 K for $\text{Ag}_{0.84}\text{Sb}_{1.16}\text{Te}_{2.16}$.

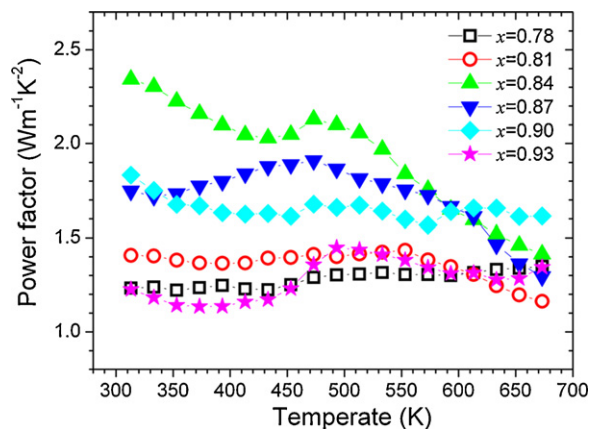


Fig. 5. Temperature dependence of power factor, PF , of $\text{Ag}_x\text{Sb}_{2-x}\text{Te}_{3-x}$ ($x = 0.78-0.93$).

It should be mentioned that the Seebeck coefficient and the electrical conductivity of the sample of $x=0.9$ annealed for 1 month have been re-measured several times to evaluate the stability of these composites. The deviation of the power factor is within 25% at low temperatures but about 10% at high temperatures. The further investigation is in progress.

The thermal conductivity is plotted in Fig. 6. All the thermal conductivities are below $0.90 \text{ W m}^{-1} \text{ K}^{-1}$. The thermal conductivities decreased with temperature. Using the Wiedemann–Franz relationship, $\kappa_e = L_0 \sigma T$, the lattice thermal conductivity κ_L can be estimated by subtracting the electronic thermal conductivity κ_e from total κ , $\kappa_L = \kappa - \kappa_e$. As plotted in Fig. 6(b), the lattice thermal conductivity decreases with temperature, indicating the U-process affecting on phonon transport. The κ_L for the double-phased samples, except $\text{Ag}_{0.93}\text{Sb}_{1.07}\text{Te}_{2.07}$, only decreased a little due to the increasing phase boundary scattering.

The figure of merit ZT values are calculated and plotted as a function of temperature in Fig. 7(a). The two single-phased samples show almost the same thermoelectric behavior. The samples with proper amounts of Ag_2Te precipitates exhibited much higher ZT over the entire temperature range. With further increasing Ag_2Te ratio, the ZT value decreased. For the $\text{Ag}_{0.93}\text{Sb}_{1.07}\text{Te}_{2.07}$, the ZT values almost decreased to the same values as those of the single-phased samples. The maximum ZT of 1.53 was obtained for $\text{Ag}_{0.84}\text{Sb}_{1.16}\text{Te}_{2.16}$ at 500 K and for $\text{Ag}_{0.90}\text{Sb}_{1.10}\text{Te}_{2.10}$ at 673 K, which is about 40% increase, compared to the single-phased samples.

As reported in our previous study [8], the Sb_2Te_3 precipitated samples with $x < 0.78$ have also been investigated. The ZT values at room temperature and 670 K of all the samples with x varying

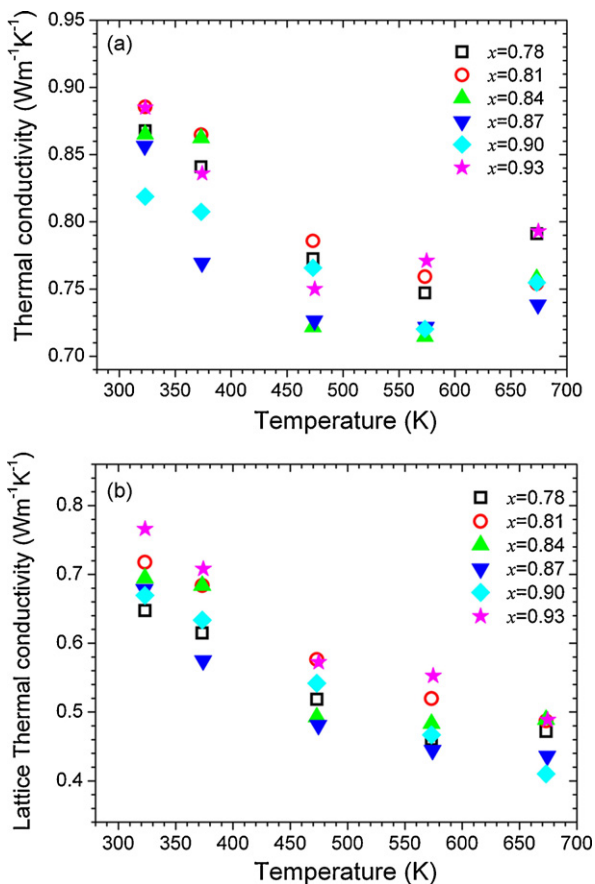


Fig. 6. Temperature dependence of thermal conductivity of $\text{Ag}_x\text{Sb}_{2-x}\text{Te}_{3-x}$ ($x=0.78$ –0.93). (a) Total thermal conductivity, κ ; and (b) Lattice thermal conductivity, κ_L .

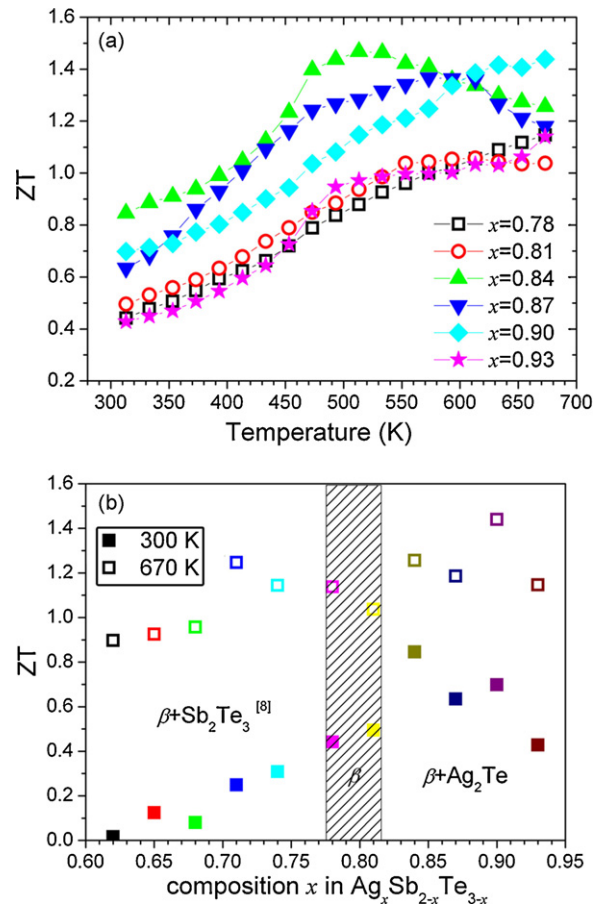


Fig. 7. (a) Temperature dependence of figure of merit ZT of $\text{Ag}_x\text{Sb}_{2-x}\text{Te}_{3-x}$ ($x=0.78$ –0.93). (b) Composition dependence of figure of merit ZT of $\text{Ag}_x\text{Sb}_{2-x}\text{Te}_{3-x}$ ($x=0.62$ –0.93). The solid and open squares represent the ZT values at 300 and 670 K, respectively.

from 0.62 to 0.93 were plotted together in Fig. 7(b). The shadowed area represents the single-phase region. As can be seen, the room temperature ZT increases with the increase of Ag_2Te ratio. While at 670 K, the increase of $\sim 10\%$ and 40% in ZT can be obtained for proper amounts of secondary phases (Sb_2Te_3 or Ag_2Te). Thus it can be suggested that by adjusting the $\text{Ag}_2\text{Te}/\text{Sb}_2\text{Te}_3$ ratio to form *in situ* nanocomposites, the thermoelectric performance of AgSbTe_2 compound can be effectively optimized.

4. Conclusions

Ternary thermoelectric semiconductor AgSbTe_2 has been synthesized with different $\text{Ag}_2\text{Te}/\text{Sb}_2\text{Te}_3$ ratios (x from 0.78 to 0.93 in $\text{Ag}_x\text{Sb}_{2-x}\text{Te}_{3-x}$). The double-phased samples with Ag_2Te secondary phase were obtained when $x > 0.81$. The HRTEM observation showed that Ag_2Te precipitated *in situ* as nanodots and nanoscale lamellas embedded in the AgSbTe_2 matrix. The thermoelectric properties have been significantly improved with proper amounts of Ag_2Te . The Seebeck coefficient and the electrical conductivity increased, resulting in the enhancement of power factor. Combining with the reduced thermal conductivity, the maximum ZT of 1.53 was obtained at 500 K for $\text{Ag}_{0.84}\text{Sb}_{1.16}\text{Te}_{2.16}$, which is a 40% increase compare to the single-phased sample.

Acknowledgements

The work is supported by the National ‘973’ Program (2007CB607502), NSFC (50731006), NSF of Zhejiang Province

(Z4090204) and the Science and Technology Program of Zhejiang Province (2009C34007).

References

- [1] D.M. Rowe, CRC Handbook of Thermoelectrics, CRC Press, New York, 1995.
- [2] T.M. Tritt, Recent Trends in Thermoelectric Materials Research, in Semiconductors and Semimetals, Academic, San Diego, 2001, p 69–71.
- [3] S. Geller, J.H. Wernick, Acta Cryst. 12 (1958) 46.
- [4] H.A. Ma, T.C. Su, P.W. Zhu, J.G. Guo, X.P. Jia, J. Alloys Compd. 454 (2008) 415.
- [5] R.W. Armstrong, J.W. Faust Jr., W.A. Tiller, J. Appl. Phys. 31 (1960) 1954.
- [6] L. Wu, J. Zheng, J. Zhou, Q. Li, J. Yang, Y. Zhu, J. Appl. Phys. 105 (2009) 094317.
- [7] K. Hoang, S.D. Mahanti, J.R. Salvador, M.G. Kanatzidis, Phys. Rev. Lett. 99 (2007) 156403.
- [8] S.N. Zhang, T.J. Zhu, S.H. Yang, C.Yu, X.B. Zhao, Acta Mater., submitted for publication.
- [9] H. Wang, J.F. Li, C.W. Nan, M. Zhou, Appl. Phys. Lett. 88 (2006) 092104.
- [10] L.H. Ye, K. Hoang, A.J. Freeman, S.D. Mahanti, J. He, T.M. Tritt, M.G. Kanatzidis, Phys. Rev. B 77 (2008) 245203.
- [11] V. Jovovic, J.P. Heremans, Phys. Rev. B 77 (2008) 245204.
- [12] R.M. Marin, G. Brun, J.C. Tedenac, J. Mater. Sci. 20 (1985) 730.
- [13] M. Salavati-Niasari, M. Bazarganipour, F. Davar, J. Alloys Compd. 489 (2010) 530.
- [14] L.D. Zhao, B.P. Zhang, J.F. Li, M. Zhou, W.S. Liu, J. Liu, J. Alloys Compd. 455 (2008) 259.
- [15] T.J. Zhu, F. Yan, X.B. Zhao, S.N. Zhang, Y. Chen, S.H. Yang, J. Phys. D: Appl. Phys. 40 (2007) 6094.
- [16] K.F. Hsu, S. Loo, F. Guo, W. Chen, J.S. Dyck, C. Uher, T. Hogan, E.K. Polychroniadis, M.G. Kanatzidis, Science 303 (2004) 818.
- [17] A.J. Zhou, T.J. Zhu, H.L. Ni, Q. Zhang, X.B. Zhao, J. Alloys Compd. 455 (2008) 255.
- [18] Y.L. Li, J. Jiang, G.J. Xu, W. Li, L.M. Zhou, Y. Li, P. Cui, J. Alloys Compd. 480 (2009) 954.
- [19] L. Zhang, A. Grytsiv, M. Kerber, P. Rogl, E. Bauer, M.J. Zehetbauer, J. Wosik, G.E. Nauer, J. Alloys Compd. 481 (2009) 106.
- [20] Q. Zhang, J. He, T.J. Zhu, S.N. Zhang, X.B. Zhao, T.M. Tritt, Appl. Phys. Lett. 93 (2008) 185103.
- [21] Y.Q. Cao, X.B. Zhao, T.J. Zhu, X.B. Zhang, J.P. Tu, Appl. Phys. Lett. 92 (2008) 143106.
- [22] J.L. Mi, X.B. Zhao, T.J. Zhu, J.P. Tu, J. Phys. D: Appl. Phys. 41 (2008) 205403.
- [23] X. Shi, L.D. Chen, S.Q. Bai, X.F. Tang, Key Eng. Mater. 249 (2003) 75.
- [24] X.Y. Huang, Z. Xu, L.D. Chen, X.F. Tang, Compos. Mater. III 249 (2003) 79.
- [25] I.U. Arachchige, J. Wu, V.P. Dravid, M.G. Kanatzidis, Adv. Mater. 20 (2008) 3638.
- [26] W.Q. Ao, W.A. Sun, J.Q. Li, F.S. Liu, Y. Du, Alloys Compd. 475 (2009) L22.
- [27] K.F. Cai, C. Yan, Z.M. He, J.L. Cui, C. Stiewe, E. Muller, H. Li, J. Alloys Compd. 469 (2009) 499.
- [28] S.H. Yang, T.J. Zhu, T. Sun, J. He, S.N. Zhang, X.B. Zhao, Nanotechnology 19 (2008) 245707.
- [29] T. Ikeda, L.A. Collins, V.A. Ravi, F.S. Gascoin, S.M. Haile, G.J. Snyder, Chem. Mater. 19 (2007) 763.
- [30] J.P. McHugh, W.A. Tiller, S.E. Hasztko, J.H. Wernick, J. Appl. Phys. 32 (1961) 1785.
- [31] R.G. Majer, Z. Metallkunde 54 (1963) 311.
- [32] K. Ståhl, Rietveld refinement framework “winpow”, Technical University of Denmark, The fitting process was based on the two lattice structures of AgSbTe₂ (JCPDS Card No. 15-0540) and Ag₂Te (JCPDS Card No.34-0142), Rwp~35.42-41.05.
- [33] J.D. Sugar, D.L. Medlin, J. Alloys Compd. 478 (2009) 75.
- [34] R.S. Allgaier, W.W. Scanlon, Phys. Rev. 111 (1958) 1029.
- [35] G.S. Nolas, J. Sharp, H.J. Goldsmid, in: R. Hull, R.M. Osgood (Eds.), Principles and New Materials Developments Thermoelectrics, Springer, 2001.
- [36] J.M.O. Zide, D. Vashaee, Z.X. Bian, G. Zeng, J.E. Bowers, A. Shakouri, A.C. Gossard, Phys. Rev. B 74 (2006) 205335.